

Durham Research Online

Deposited in DRO:

12 December 2016

Version of attached file:

Accepted Version

Peer-review status of attached file:

Peer-reviewed

Citation for published item:

Underwood, T. and Erastova, V. and Greenwell, H.C. (2016) 'Ion adsorption at clay mineral surfaces : the Hofmeister series for hydrated smectite minerals.', *Clays and clay minerals.*, 64 (4). pp. 472-487.

Further information on publisher's website:

<https://doi.org/10.1346/CCMN.2016.0640310>

Publisher's copyright statement:

Additional information:

Use policy

The full-text may be used and/or reproduced, and given to third parties in any format or medium, without prior permission or charge, for personal research or study, educational, or not-for-profit purposes provided that:

- a full bibliographic reference is made to the original source
- a [link](#) is made to the metadata record in DRO
- the full-text is not changed in any way

The full-text must not be sold in any format or medium without the formal permission of the copyright holders.

Please consult the [full DRO policy](#) for further details.

Ion Adsorption at Clay Mineral Surfaces: The Hofmeister Series for Hydrated Smectite

Minerals

Thomas Underwood, Valentina Erastova, H. Chris Greenwell

Durham University

Department of Earth Sciences,

Durham University,

Science Labs,

Durham DH1 3LE

ABSTRACT

Many important properties of clay minerals are defined by the species of charge-balancing cation. Phenomena such as clay swelling and cation exchange depend upon the cation species present and it is therefore important to understand how the cations bind with the mineral surface at a fundamental level. In the present study, the binding affinities of several different charge-balancing cations with the basal surface of the smectite clay montmorillonite have been calculated using molecular dynamics in conjunction with the well-tempered metadynamics algorithm. The results follow a Hofmeister series of preferred ion adsorption to the smectite basal surfaces of the form:

$$\text{K}^+ > \text{Na}^+ > \text{Ca}^{2+} > \text{Cs}^+ > \text{Ba}^{2+}$$

The results also reveal the energetically favorable position of the ions above the clay basal surfaces. Key features of the free energy profiles are illustrated by Boltzmann population inversions and analyses of the water structures surrounding the ion and clay surface. The results show that weakly hydrated cations (K^+ and Cs^+) preferentially form inner-sphere surface complexes (ISSC) above the ditrigonal siloxane cavities of the clay, whilst the more strongly hydrated cations (Na^+) are able to form ISSCs above the basal oxygen atoms of the clay surface. The strongly hydrated cations (Na^+ , Ca^{2+} and Ba^{2+}) preferentially form outer-sphere surface complexes. The results provide insight into the adsorption mechanisms of several ionic species upon smectite clay minerals, and are relevant to many phenomena thought to be affected by cation-exchange, such as nuclear waste disposal, herbicide/pesticide-soil interactions and enhanced oil recovery.

- 31 *Keywords:* Binding affinity; cation exchange; molecular dynamics; montmorillonite; well-
32 tempered metadynamics.

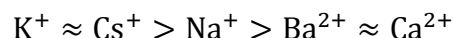
INTRODUCTION

Clays are naturally occurring layered phyllosilicate minerals which are known to play an important role in many geochemical processes, whether within marine systems, terrestrial soils or within the subsurface in aquifers and oil reservoirs (Bergaya *et al.*, 2006). Owing to their high surface area, permanent negative charge and cation exchange properties, smectite clay minerals have found an increasing multitude of practical applications and have been extensively studied using analytical laboratory based techniques. In recent years, computational techniques, such as molecular dynamics (MD) and *ab-initio* calculations (including density functional theory – DFT), have become increasingly beneficial in helping improve our understanding of clay mineral properties at the atomistic level ((Greenwell, 2006), (Suter J. L., 2009)).

Three types of clay mineral surfaces are apparent: (i) the external basal surfaces, (ii) the external clay edges; (iii) the interlayer basal surfaces. The adsorption and exchange of cations at the different clay minerals surfaces can comprehensively alter the physical and chemical properties of the clay mineral. Interlayer bound potassium, for example, acts as a swelling inhibitor, preventing hydration and expansion of the interlayer region, whilst sodium promotes swelling when present in smectite-like clay minerals (Boek *et al.*, 1995). Furthermore, owing to their use as a barrier material in underground nuclear waste repositories it is becoming increasingly important to understand how radioactive cations, such as barium and cesium, adsorb to clay mineral surfaces, with potentially significant ramifications for nuclear waste repository design and operation (Ngouana *et al.*, 2014). Since the behavior of clay minerals depend upon the species of charge-balancing cation, it is important to understand how the cation binds with the mineral surface, and how the cation's affinity to the surface differs from ion to ion; however, studying the behaviour of cations at clay mineral surfaces and within interlayers is particularly

challenging. Nuclear magnetic resonance (NMR) studies have been undertaken on non-paramagnetic synthetic clays offering insight on ion dynamics and distribution (Bowers *et al.*, 2008), while the use of quasi-elastic neutron scattering (QENS) on well-ordered vermiculite clay gels, as well as smectites, has allowed the study of cation/water structure in interlayers ((Swenson *et al.*, 2000), (Marry *et al.*, 2013)). Additional insight into swelling energetics and structure has been obtained from computer simulation of hydrated clay minerals ((Boek *et al.*, 1995), (Shroll and Smith, 1999), (Boek and Sprik., 2003)).

A key property of many clay minerals is cation-exchange, where a more labile cation is substituted by a less labile one to modify the clay mineral activity. The traditional view of alkaline metal ion selectivity for cation-exchange follows a Hofmeister-like series (Hanshaw, 1964):



The reasoning for this sequence have been postulated through (at least) two arguments:

- 1) The ratio of hydrated cation size to interlayer spacing ((Gast, 1969), (Gast, 1972)), whether the hydrated ion can fit within the steric cavities of the interlayer spacing;
- 2) The cations' ability to partially dehydrate at the mineral surface and thus form strong inner-sphere surface complexes (Eisenman, 1962).

Whilst many historical studies of the Hofmeister series have examined the hydration properties of the ions, in recent years it has become increasingly apparent that ion-macromolecule interactions also play a dominant role (Zhang and Cremer, 2006). Previous computational work has been able to elucidate some of the properties of cation-exchange clay systems. It has previously been shown that whilst the binding energy between

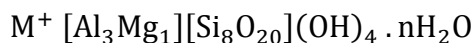
potassium and montmorillonite is greater than that between cesium and montmorillonite, the cesium-montmorillonite system is overall more stable due to the decreased enthalpy of hydration of the potassium over the cesium in the solvent phase (Teppen and Miller, 2006). The result shows it is important to consider not only the effect of the ion interacting with the mineral surface, but also with the bulk solvent phase. Previously, this has been achieved using an explicit solvent bath (Rotenberg *et al.*, 2007) or through the use of thermodynamic cycles (Rotenberg *et al.*, 2009).

In this present study, classical molecular dynamic simulations have been used in conjunction with well-tempered metadynamics to determine the free energy of adsorption of, as well as the competition between, cations at the hydrated basal surfaces of the smectite clay mineral montmorillonite. The following simulations are particularly pertinent for understanding of the phenomenon of multicomponent cation-exchange during low salinity enhanced oil recover, whereby organic matter, bridged to the surface through divalent cations, becomes desorbed from the basal surface of a clay mineral (Underwood *et al.*, 2015).

METHODS

Model Setup

The clay unit cell used in this study was a Wyoming-like montmorillonite with atomic coordinates taken from the *American Mineralogist Crystal Structure Database* ((Downs and Hall-Wallace, 2003), (Viani *et al.*, 2002)) and with stoichiometry:



In this model the octahedral sheets of the clay contained one Mg atom for every three Al atoms, whilst both tetrahedral sheets contained no isomorphic substitutions. The resulting unit cell possessed a single net negative charge, corresponding to a surface charge density of approximately 0.35 C m^{-2} . Periodically replicated super-cells were generated containing one layer of montmorillonite, composed of 18 unit cells ($6 \times 3 \times 1$), with dimensions of approximately $30 \times 30 \times 100 \text{ \AA}$, and a pore-spacing of approximately 90 \AA (Figure 1). Montmorillonite structures initially occupied the region $0 < z < 7 \text{ \AA}$ in all the following simulations, and the clay position varied little over all timescales modelled. The simulation super-cells were subsequently hydrated (with approximately 2500 water molecules) and the requisite number of cations added to the system to charge balance the montmorillonite surface. In total, five independent systems were set up differing according to the type of charge-balancing cation. The cations considered in this study were: sodium (Na^+), potassium (K^+), cesium (Cs^+), calcium (Ca^{2+}) and barium (Ba^{2+}).

The clay mineral has been modelled using the ClayFF force field (Cygan *et al.*, 2004), which is specifically parameterized to model layered minerals. The ClayFF force field is designed such that the entire interactions within, and structure of, the clay is described wholly by the non-bonded Lennard-Jones and Coulomb potentials (hydroxyl groups are bonded as an

exception). The standard SPC water model (Berendsen *et al.*, 1987) has been used to parameterize the solvent. Ion parameters are taken from a variety of sources and are consistent with the ClayFF and SPC force fields ((Smith and Dang (I), 1994), (Smith and Dang (II), 1994) (Koneshan *et al.*, 1998),(Aqvist, 1990)), (Cygan *et al.*, 2004).

Equilibration Details

All simulations have been initialized with an energy minimization run to reduce any excessive force on any one atom. This was accomplished using a steepest descents algorithm, with convergence achieved once the maximum force on any one atom was less than $10 \text{ kJ mol}^{-1} \text{ \AA}^{-1}$. Subsequently, equilibration simulations were run for a 10 ns period in the constant number of particles, pressure and temperature (NPT) ensemble at 300 K and 1 bar using a velocity-rescale Berendsen thermostat, temperature coupling constant set to 0.1 ps, and a semi-isotropic Berendsen barostat, with pressure-coupling constant 1 ps. The Berendsen thermostat and barostat offered swift equilibration of the system, and convergence was adjudged to have been attained once both the z -spacing and potential energy had converged.

Metadynamic Details

Subsequent to equilibration, the super-cell was translated along the z -axis such that the apical oxygen atoms of the silicate sheet of the lowest clay basal surface lay upon the $z = 0 \text{ \AA}$ plane. Before any free energy calculations were carried out, the clay model was fixed in place as a rigid structure. Subsequently, a single cation was chosen at random to be the test ion, upon which the free energy calculations have been performed. All other ions in the system were free to move according to the force fields used in the simulations.

The well-tempered metadynamics algorithm was used to explore the free energy curve of the clay-ion-water system as a function of the clay-ion separation (i.e. the reaction coordinate). During the metadynamics simulation the forces calculated with conventional molecular dynamics are modulated by adding Gaussian functions to the Hamiltonian at points along the reaction coordinate (Barducci *et al.*, 2008). Here, twenty-five separate well-tempered metadynamic simulations were run, five for each cation type. It is important to run multiple ensemble simulations when calculating equilibrium thermodynamic properties, such as binding energies, since any one simulation is unlikely to sufficiently sample all of the phase-space required to satisfy the ergodic hypothesis (Coveney and Wan, 2016). Five separate ensemble simulations were deemed sufficient to reduce the total uncertainty in the free energy profiles generated using the metadynamic algorithm in this work. Each metadynamic simulation was run for a duration of 200 *ns* at 300 *K* in the constant number of particles, volume and temperature (NVT) ensemble. Gaussian functions with an initial height of 1.20 *kJ/mol*, a width of 0.10 Å, and a bias factor of 10 were applied to the Hamiltonian every 0.5 *ps*. Convergence of the well-tempered metadynamics algorithm was ensured by observing that the Gaussian height tended to zero throughout all well-tempered metadynamic simulations. Checks were also made to ensure that the test ion sampled all of the available planar *xy*-space, in conjunction with clay-ion separation space.

Due to the translational symmetry of the clay mineral, additional bias potentials were added to the test ion. This constrained the ion within a single unit cell of the montmorillonite surface. Any additional sampling would simply increase computational time, yet yield no additional information. This constraint was achieved using a spring-like bias of the form:

$$V_{\text{wall}}(x) = k(x - x_{\text{max}})^4 \quad \text{for } x > x_{\text{max}} \quad (1)$$

where k is the elastic spring constant of the wall, set to 500 kJ/mol , and x_{max} is the lower limit of the wall. Similar boundaries were setup to constrain the lower bounds of the test ion in the x -direction, to constrain the ion in the y -direction, as well as to keep the test ion within 10 \AA of the mineral surface.

Simulation Details

All MD simulations were performed using GROMACS version 4.6.7 (Pronk, et al., 2013) with the Particle-Mesh-Ewald summation method for determining the electrostatic contribution, with a real-space electrostatic cut-off of 12 \AA , a reciprocal space precision of 10^{-5} , in addition to a van der Waals cut-off distance of 1.2 \AA . The well-tempered metadynamic algorithm has been implemented using PLUMED 2.1.2 (Bonomi *et al.*, 2009) (Tribello *et al.*, 2014), which works in conjunction with GROMACS, whilst all images of the simulated structures have been produced using VMD 1.9.2 (Humphrey, 1996).

Analysis Details

All free energy analyses have been carried out using the internal tools for GROMACS 4.6.7 and PLUMED 2.1.2 (Bonomi *et al.*, 2009) (Tribello *et al.*, 2014). The Python module MDAnalysis 0.13 (Michaud-Agrawal *et al.*, 2011) and Matplotlib 1.5.1 (Hunter, 2007) were used to further analyze simulation trajectories and generate figures of water densities and radial distribution functions (RDFs). The plotted free energy profiles present the average free energy at each point along the reaction coordinate as a bold line and the relative error (plus-minus) is presented in the shaded area. The values of individual binding energies are given with the corresponding standard error as plus-minus. All ion density profiles (dotted lines in the free

183 energy profiles) have been calculated using the last 5 *ns* of the 10 *ns* equilibration period, i.e.
184 from an unbiased simulation.

RESULTS

It is initially worth highlighting the general shape of the free energy curves (Figure 2).

After a short range repulsion between ion and mineral surface, and beyond (often several) minima, the free energy profiles plateau. In the long clay-ion separation limit, this plateau can be decomposed as a combination of clay ($F_{\text{self}}^{\text{clay}}$), ion ($F_{\text{self}}^{\text{ion}}$) and solvent ($F_{\text{self}}^{\text{water}}$) self-energies; clay-water ($F_{\text{hydration}}^{\text{clay}}$) and ion-water ($F_{\text{hydration}}^{\text{ion}}$) hydration energies; as well as long-range interaction terms ($F_{\text{electrostatic}}^{\text{clay-ion}}$). Namely the binding free energy (F), can be expressed as:

$$\lim_{z \rightarrow \infty} F(z) = F_{\text{self}}^{\text{clay}} + F_{\text{self}}^{\text{ion}} + F_{\text{self}}^{\text{water}} + F_{\text{hydration}}^{\text{clay}} + F_{\text{hydration}}^{\text{ion}} + F_{\text{electrostatic}}^{\text{clay-ion}}(z) \quad (2)$$

This means that the overall binding energy ($\Delta F_{\text{Binding}}$) of the ion to the surface can be calculated as:

$$\Delta F_{\text{Binding}} = F(z_{\text{min}}) - \lim_{z \rightarrow \infty} F(z) \quad (3) \text{ where } z_{\text{min}} \text{ is the location of the global energy}$$

minimum with respect to clay-ion separation.

Note that at sufficiently large z , the individual self-energies of the unbound system and hydration terms in equation 2 are independent of z , since the hydration shells of the ion and clay no longer overlap. Thus, at large z , when comparing binding energies between different ion species, one needs only to consider the difference between the long-range clay-ion electrostatic term. Since all simulations have been run at the same temperature (300 K) and ionic strengths the long-range electrostatic term, which can be described through Poisson-Boltzmann theory, is postulated to be equal for all different ions at any arbitrary z . It is therefore justified to normalize the free energy profiles subject to the boundary condition that for large clay-ion separation:

$\lim_{z \rightarrow \infty} F(z) = 0$ (4) Following this argument, a direct comparison of the binding free energies differences between dissimilar species of monovalent and divalent cations have been calculated (Table 1).

Free Energy Profiles:

The free energy profile for all the systems considered (Figure 2), highlight several points of interest along the reaction-coordinate. These are highlighted by the points (A), (B), (C), (D) and (E) across the top of the figure. To be consistent, the points correspond to the coordination states of the ion. In brief, (A) corresponds to a primary inner-sphere surface complex (ISSC); (B) corresponds to a secondary ISSC; (C) corresponds to outer-sphere surface complex (OSSC) and (D) corresponds to a secondary hydration shell surface complex (SHSSC). These terms shall be explained in the following sections. The point (E) corresponds to a clay-ion separation of 10 Å, the maximal distance of the reaction-coordinate in the metadynamic simulations.

Na-Montmorillonite:

The free energy profile for the sodium-montmorillonite system (Figure 2 - Na) shows that at close separation distances (less than 2 Å) the montmorillonite-ion interaction is entirely repulsive. This represents the close-range repulsion between clay and ion due to electron wave-function overlap. Beyond this, the ion experiences three individual clay-ion separations of (meta)stable equilibria. The global minimum, and thus the most energetically favorable montmorillonite-sodium separation is at 3.8 Å, with a binding energy of -9.00 ± 0.35 kJ/mol (Figure 2 – Na(C)). A secondary, metastable minimum, is located nearer to the clay surface, at a clay-sodium distance of 2.3 Å, with a binding energy of -2.76 ± 0.43 kJ/mol (Figure 2 - Na(B)). A

third, metastable minimum, is located further from the clay surface, at a separation value of 6 Å and with a binding energy of -3.68 ± 0.37 kJ/mol (Figure 2 - Na(D)).

The global minimum corresponds to a system where the sodium cation is fully hydrated, and the ion's solvation shell is associated to the mineral surface *via* hydrogen bonding. This can be observed in the overlapping water structures of the first hydration shell of the ion with the first hydration layer of the clay (Figure 3 - Na(C)). This phenomenon is well known, and referred to as an outer-sphere solvation complex (OSSC). In contrast, the metastable minimum nearer the clay surface corresponds to an inner-sphere solvation complex (ISSC), whereby the cation is only partially hydrated, and is directly adsorbed to the mineral surface *via* electrostatic interactions (Figure 3 - Na(B)). The metastable minimum farthest away from the clay surface corresponds to where the second hydration shell of the sodium ion overlaps with the first hydration layer of the clay (Figure 3 - Na(D)). This situation is observed for several cations and shall be hereafter denoted as a secondary hydration shell surface complex (SHSSC). Also presented is the water structure surrounding the ion and clay at a clay-ion separation of 10 Å (Figure 3 - Na(E)). It can be noted that at such distance, the hydration layers of the clay and ion no longer overlap.

The radial distribution functions (RDFs) between sodium ion and water/basal clay oxygen further reiterate that the minima correspond to ISSC and OSSC. It can be seen that for the ISSC (Figure 4 - Na(B)), the basal clay oxygen atoms are shared with water oxygen atoms in the first coordination shell of the ion. In contrast, for the OSSC (Figure 4 - Na(C)), the basal clay oxygen atoms are contained within the second coordination shell of the ion. For the SHSSC (Figure 4 - Na(D)), the clay basal oxygen atoms contribute to the third coordination shell of the sodium ion. Also presented is the RDF for the system at a clay-ion separation of 10 Å (Figure 4 -

Na(E)). In this case the hydration layers of the ion and clay no longer interact and the resulting RDF is that of the sodium ion with bulk water.

The planar density of the ion above the mineral surface shows that, for the ISSC, the sodium ion is extremely localized above a single basal clay oxygen (Figure 5 - Na(B)). In contrast, the OSSC is less localized above the clay basal surface (Figure 5 - Na(C)), with a preference to be located above one of the hexagonal siloxane cavities of the mineral surface. For the SHSSC and beyond, the ion's position above the basal clay surface is no longer localized, and is homogeneously dispersed across the unit cell (Figure 5 - Na(C) and Na(D)).

K-Montmorillonite:

The free energy profile for potassium (Figure 2 - K) presents several features similar to that of sodium. Again, it can be seen that beyond the typical close distance repulsion, three separate (meta)stable minima are observed. The global minimum, in this instance, is located near the surface of the mineral, at a montmorillonite-potassium separation of 1.3 Å, with a binding energy of -10.56 ± 1.29 kJ/mol (Figure 2 - K(A)). The next most stable minimum is located at 4.7 Å, with a binding energy of -3.83 ± 0.37 kJ/mol (Figure 2 - K(C)). There is also a metastable minimum between these two points at a clay-potassium separation of 2.6 Å with a binding energy of -2.46 ± 0.70 kJ/mol (Figure 2 - Na(B)).

Focusing on the global energy minimum (point A), both the water structure (Figure 3 - K(A)) and the RDF (Figure 4 - K(A)) reveal that the ion forms an ISSC in its most energetically favorable state. In particular, the RDF shows that the first coordination shell of the potassium ion is largely composed of clay oxygen atoms. The xy-planar density of the potassium ion in its ISSC state (Figure 5 - K(A)) shows that the ion is extremely localized above the hexagonal cavities of

the clay surface. This behavior is in contrast to the ISSC observed for sodium. The terms primary ISSC and secondary ISSC are here introduced to denote the difference between these two different forms of ISSC. A primary ISSC denotes an ion that sits above one of the hexagonal cavities of the clay surface, whilst the term secondary ISSC denotes that the ion sits above one of the basal oxygen atoms of the clay.

The least energetically favorable metastable minimum is located at point (B) in the free energy profile (Figure 2 – K(B)). The water structure (Figure 3 - K(B)) and RDF (Figure 4 – K(B)) indicate that this minimum is also an ISSC. The xy -planar density of the ion above the surface (Figure 4 - K(B)) indicates that this is a secondary ISSC. The results show that potassium can stably form both primary, and secondary, inner-sphere surface complexes.

The most energetically favorable metastable minimum is located at point (C) in the free energy profile (Figure 2 – K(C)). Here the potassium ion forms an OSSC, as the first hydration shell of the ion overlaps with the first hydration layer of the clay (Figure 3 - K(C)). The RDF (Figure 4 - K(C)) also highlights that the basal clay oxygen atoms coordinate within the second hydration shell of the potassium cation. Like the sodium ion, the OSSC of potassium is loosely localized above the hexagonal siloxane cavities of the basal surface, as evidenced by the xy -planar density distribution (Figure 5 - K(C)). Beyond this point, the potassium ion is not observed to form a SHSSC and moves freely across the xy -plane (Figure 5 - K(E)).

Cs-Montmorillonite:

The free energy diagram for the cesium-montmorillonite system (Figure 2 - Cs) is very similar to that of potassium. Again, three separate minima are observed. The global energy minimum is at a montmorillonite-cesium separation of 2.0 Å with a binding energy of -

8.34±0.40 *kJ/mol* (Figure 2 - Cs(A)). The secondary minimum is at a clay-ion distance of 2.7 Å with a binding energy of -7.51±0.38 *kJ/mol* (Figure 2 - Cs(B)) and the tertiary minimum is located at a clay-ion distance of 4.6 Å with a binding energy of -4.64±0.26 *kJ/mol* (Figure 2 - Cs(C)).

The global minimum of cesium forms an ISSC as can be observed through the water structure (Figure 3 - Cs(A)) and cesium-oxygen RDF results (Figure 4 - Cs(A)). Like potassium, the global energy minimum of cesium is localized above the hexagonal siloxane cavities of the clay surface (Figure 5 - Cs(A)) and is therefore observed to form primary ISSCs.

The second and third minima of cesium correspond to a secondary ISSC and OSSC respectively. This is evidenced by the overlapping of the water structures surrounding the ion and clay (Figure 3 - Cs (B) and Cs(C)), the overlapping oxygen atoms in the RDFs (Figure 4 - Cs(B) and Cs(C)), as well as the ion localizations above the *xy*-plane (Figure 5 - Cs(B) and Cs(C)). Much like potassium therefore, cesium readily forms both secondary ISSCs and OSSCs. Unlike potassium however, the secondary ISSC is more energetically stable than the OSSC.

Ca-Montmorillonite:

In contrast with the results for other ions presented so far, the free energy profile for calcium shows only one stable minimum (Figure 2 – Ca). This minimum is at a clay-ion distance of 3.8 Å and has a binding energy of -16.76±0.41 *kJ/mol* (Figure 2 - Ca(C)). The water structures surrounding the calcium and clay in conjunction with the RDFs between ion and oxygen atoms show that this global energy minimum is an OSSC. The water structure (Figure 3 – Ca(C)) shows that the first hydration shell of the calcium overlaps with the first hydration layer of the clay basal surface. Furthermore, the RDF (Figure 4 - Ca(C)) indicates that the basal oxygen

atoms of the clay contribute to the second hydration shell of the calcium. The planar density of the calcium ion in its global OSSC state (Figure 5 - Ca(C)) presents that the calcium ion sits above the hexagonal siloxane cavities of the basal surface of the clay, in agreement with the trends observed for the monovalent ions. Nonetheless, the OSSC for the calcium ion is more localized compared to the OSSCs for monovalent ions.

Point (D) in the calcium system refers to the sudden change in gradient of the free energy curve. This change in gradient is due to the completion of the second hydration shell of the calcium ion as is shown in the water density profile (Figure 3 - Ca(D)). At this point the clay no longer contributes to the hydration shells of the calcium ion, as is confirmed by comparing the RDF between calcium and basal clay oxygen atoms with the RDF between calcium and all oxygen atoms (Figure 4 - Ca(D)). The planar density profile for point (D) (Figure 4 - Ca(D)) shows that calcium ion sits above the either the basal oxygen of silicon atoms of the clay. Therefore, the aforementioned completion of the second coordination shell of the calcium ion is achieved with water oxygen atoms.

Ba-Montmorillonite:

The free energy profile of the montmorillonite-barium system (Figure 2 - Ba) presents several interesting features not observed in the free energy profile for calcium. The global energy minimum (point C) corresponds to a clay-ion separation of 4.2 Å with a binding energy of -16.66±1.46 kJ/mol (Figure 2 - Ba(C)). There is also a second, energetically expensive, metastable minima in the free energy curve (point A). This metastable minimum is located at a clay-ion separation value of 1.9 Å and has a binding energy of +18.26±3.55 kJ/mol (Figure 12 - Ba(A)), i.e. energy is required to place the ion into this metastable minimum. Two plateaus can

also be seen in the free energy profile of barium. Point (B) is at a clay-ion separation of 2.6 Å and has a binding energy of -0.54 ± 1.82 kJ/mol (Figure 2 - Ba(B)), whilst point (D) is at a clay-ion separation of 5.8 Å and has a binding energy of -8.38 ± 1.25 kJ/mol (Figure 2 - Ba(D)).

The water density profiles and RDFs of the barium-montmorillonite system explain how the ion binds with the mineral surface. At points (A) and (B), the ion is directly coordinated by basal oxygen atoms, forming primary and secondary ISSCs respectively (Figures 3 and 4 – Ba(A) and Ba(B)). The water structure shows that the global energy minimum occurs when the barium ion is an OSSC (Figure 3 - Ba (C)). In such an occurrence, the basal oxygen atoms of the clay contribute to the second hydration shell of the cation, as can be seen in the corresponding RDF (Figure 4 - Ba(C)). The plateau at point (D) of the free energy curve occurs when the second hydration layer of the barium ion begins to completely coordinate with water oxygen atoms (Figure 3 - Ba(D)).

Analysis of the planar density of barium above the *xy*-plane of the clay shows that the two ISSCs are extremely localized above a cavity of the clay siloxane (Figure 5 - Ba (A)) or directly above basal oxygen atoms (Figure 5 - Ba (B)) for the metastable minimum (point A) and plateau (point B) respectively. Similar to all other OSSCs, the OSSC of barium is localized above one of the hexagonal siloxane cavities of the clay (Figure 5 - Ba (C)), whilst at all clay-ion separations greater than this distance, the cation freely traverses across the *xy*-plane of the clay mineral (Figure 5 - Ba (D)).

DISCUSSION

The results show that the charge-balancing cations of montmorillonite can form four different stable surface complexes: a primary ISSC located above the siloxane cavity of the basal

clay surface; a secondary ISSC located above a basal oxygen atom; an OSSC loosely located above siloxane cavity; and a SHSSC, which is due to the overlap of the ion's second hydration sphere with the clay minerals first hydration layer. No further surface complexes were observed in the simulations.

The formation of two separate ISSCs has been noted in the literature previously. In particular, it has been shown that weakly hydrated interlayer cations (K^+ , Cs^+) form ISSCs above the siloxane cavity of the clay interlayer ((Park and Sposito, 2002), (Nakano *et al.*, 2003), (Marry and Turq, 2003)) whilst strongly hydrated cations (Na^+) form ISSCs on tetrahedral charge sites ((Boek *et al.*, 1995), (Chang *et al.*, 1995), (Marry and Turq, 2003)). The results presented here supplement this previous work, and further suggest that the formation of ISSCs for strongly hydrating cation can occur in the absence of tetrahedral charge substitutions. Moreover, they implicate that the formation of different surface complexes is related to the hydration properties of the cation. The stable surface complexation of a cation is related to the hydrated radii of the atom, which is, in turn, inversely proportional to the charge/size ratio of the ion (Table 2).

The weakly hydrated cations, K^+ and Cs^+ , have very similar hydration radii (Table 2), and therefore exhibit similar behavior. In both cases, the primary ISSC is the most energetically favorable state of the ion, and the secondary ISSC and OSSC are metastable. The strongly hydrated monovalent cation, Na^+ , forms secondary ISSCs, OSSCs and SHSSCs, and is energetically most stable in its OSSC. Similarly, divalent cations form globally stable OSSCs, in concordance with the relevant literature ((Brown and Kevan, 1988), (Papelis and Hayes, 1996), (Chen and Hayes, 1999), (Strawn and Sparks, 1999), (Greathouse *et al.*, 2000)). Barium exhibits interesting behaviour; it is an ion that can form stable primary ISSCs and OSSCs, with plateaus in the free energy profile associated with the formation of a secondary ISSC and a SHSSC

(Zhang *et al.*, 2001). This is due to the larger atomic radius of barium compared to calcium, whereby the charge/size ratio of barium lies somewhere between that of calcium and sodium.

Overall, the results are well converged. The largest errors encountered are for the free energy profiles of potassium and barium. Since the free energy profile for barium contains several plateaus and minima, the metadynamic algorithm requires more simulation time to sample all clay-ion separation phase space compared to other ions. The potassium ion contains a large error due to the lack of convergence in the global energy minimum. This is due to the complex coordination of oxygen atoms to the potassium ion, and shall be elaborated upon further in the following sections.

Accuracy of Results:

To further analyze the accuracy of the free energy profiles, a comparison is made between the equilibrium density profile of the unbiased equilibration simulation with the density profile derived from the free energy. The cation density surrounding the montmorillonite surface is derived from the free energy profile as:

$$n(d) \propto \exp\left(\frac{-\Delta G(d)}{k_B T}\right) \quad (5) \text{ where } n(d) \text{ is the density profile of the ion}$$

surrounding the clay, $\Delta G(d)$ is the corresponding free energy at the point d and $k_B T$ is the thermal energy at temperature T . Strictly speaking, since the simulations have been carried out in the NVT ensemble, the calculated free energy is the Helmholtz free energy. However, because the simulations had been previously equilibrated in the NPT ensemble, one can assume that the Helmholtz and Gibbs free energies are equivalent, under the assumption that the metadynamic bias applied to the ion does not alter the average z -spacing of the simulation box.

The analysis shows that the free energy profiles capture the overall trends observed in the unbiased density profile (Figure 6). In particular, the strongly hydrating cations (Na^+ , Ca^{2+} and Ba^{2+}) density profiles match extremely well. The free energy profiles generated for Na^+ , Ca^{2+} and Ba^{2+} capture the essential details of the equilibrium density profile and agrees with previous results of cationic distribution surrounding montmorillonite basal surfaces (Rotenberg *et al.*, 2010) (Greathouse *et al.*, 2015). The ion densities calculated from the free energy profiles for the weakly hydrating cations (K^+ and Cs^+) vary considerably compared to the equilibrium density. In the case of potassium, the metadynamic density underestimates the the proportion of secondary ISSCs and OSSCs, suggesting that the free energy calculation overestimates the global binding energy of potassium to montmorillonite. In contrast, the metadynamic density overestimates the proportion of secondary ISSCs and OSSCs for cesium. This suggests that the free energy profile underestimates the global binding energy of cesium. Clearly, there is a phenomenon occurring for the weakly hydrated cations, causing their binding energies to be less accurate compared to their more strongly hydrated counterparts.

Coordination Analysis

The lower accuracy in the binding energies for potassium and cesium can be explained by examining the coordination number of the ion in its most energetically stable state. This is calculated by integrating under the first peak of the radial distribution function (RDF) for each ion (Table 3). Note that in bulk, the coordination of ions ranges between 6 to 8 oxygen atoms, systematically 1 to 2 counts over the expected literature values (Varma, 2006). In the SHSSC and OSSC states, the ion remains completely coordinated with water oxygen atoms. In the secondary ISSC the strongly hydrated sodium ion is coordinated by five water oxygen atoms and

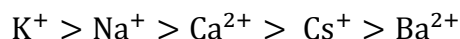
one clay oxygen atom. This, along with the xy -planar density for sodium in its ISSC, proves that the strongly hydrated monovalent cation coordinates directly above a single basal clay oxygen atom. The coordination of the secondary ISSCs for the weakly hydrating cations, potassium and cesium, show that 2 to 3 clay oxygen atoms are contained within the ions first coordination shell. The secondary ISSCs for potassium and cesium complex with a triad of basal oxygen atoms, in keeping with previous literature (Park and Sposito, 2002).

Profoundly, for the primary ISSC of potassium and cesium, the ion is coordinated with six oxygen clay atoms, as well as four/six water oxygen atoms. This drastic change in the total coordination number of potassium and cesium is the reason that the binding energy calculations are less precise for these ions. It is believed that the structure of the basal siloxane surface is formed of ditrigonal cavities (Tesson *et al.*, 2016), rather than the hexagonal cavities observed in these simulations. This suggests a limitation in the force field used within these calculations. The recently developed polarizable force field (Tesson *et al.*, 2016) is parameterized to accurately reproduce the ditrigonal structure of a clay mineral surface, and may be a more suitable choice going onwards with further binding energy calculations. Also, the Interface force field (Heinz *et al.*, 2013) which includes explicit bonding between surface atoms and dissimilar atom types for basal oxygen atoms, may be more suited to this task.

Equilibrium Constants and Determining a Hofmeister Series for the basal surface of Montmorillonite:

To compare binding energies between divalent and monovalent cations at basal surfaces it is required to divide the divalent binding affinity by two (or double the monovalent value) since it takes two monovalent ions to replace a single divalent ion in identical clay systems. This

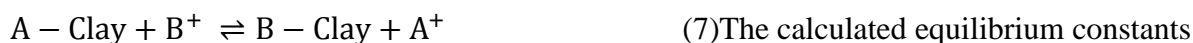
is valid assuming that the chemical environments of the two monovalent ions do not overly interact with one another. Following this procedure, the results present a Hofmeister-like series for ion adsorption to smectite mineral surfaces of the form:



Furthermore, the binding energy difference between ion A and B ($\Delta\Delta G_A^B$) can be tabulated by considering the difference in global binding energies between the respective atoms (Table 4). These values are related to the exchange equilibrium constant ($^{ex}K_A^B$) as (Bourg and Sposito, 2011):

$$\Delta\Delta G = -RT \ln(K) \quad (6) \text{ where } ^{ex}K_A^B \text{ relates to the equilibrium reaction}$$

between clay, cation A and cation B:



generally agree with the literature values (Table 5). The $\Delta\Delta G_A^B$ binding energy differences are of the order of the thermal energy at 300K (2.476kJ) or smaller in all instances. Overall, the values of K_A^B and $\Delta\Delta G_A^B$ show that the basal surface of montmorillonite is weakly selective, in agreement with literature results (Bourg and Sposito, 2011).

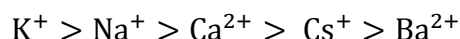
CONCLUSIONS

In this study multiple ensembles of molecular dynamic simulations used in conjunction with well-tempered metadynamics, have been used to form the basis for deriving the adsorption energies and mechanisms of simple ions to hydrated mineral surfaces. The methodology is robust and can be transferred to a wide variety of applications to measure the affinity between mineral surfaces and a marked assortment of organic material. The results immediately suggest further ways to improve the accuracy of the calculation of binding energies to clay mineral surfaces.

When calculating the binding energy of poorly hydrating molecules to clay surfaces, such as potassium and cesium, it is critically important to accurately portray the ditrigonal coordination of basal surface oxygens on the siloxane surface.

Detailed analysis of the water structure and planar xy density of cations in their energetically favorable states has revealed four separate surface-ion complexations. Both primary and secondary ISSCs are observed for the weakly and strongly hydrated cations respectively. A second hydration shell surface complex, whereby the second hydration shell of the cation overlaps with the first hydration layer of the mineral surface, is observed for sodium. Outer-shell surface complexes are observed to form for the strongly hydrated ions, sodium, barium and calcium.

Using the metadynamic algorithm, the results have confirmed the idea of a Hofmeister series for smectite-like minerals. For basal surfaces, the series follows the form:



and this insight impacts upon a wide range of industrial applications of clay minerals. Finally, the preference for monovalent ions to be adsorbed to the surface over the naturally occurring divalent ions is important for many industrial applications using the cation-exchange mechanism, whereby an inherently present divalent calcium ion is replaced with monovalent cation which can improve, for example, water-wettability, and thus increase oil extraction rates in enhanced oil recovery. Future work entails studying the adsorption of ions as a function of salt concentration, the energetics of intercalated ions as well as the calculating the energy barriers at clay edge sites. Furthermore, the role of tetrahedral substitutions may play a large role in the stability of such ionic systems.

501 ACKNOWLEDGEMENTS

502 The authors thank BP for funding Thomas Underwood, the Leverhulme Foundation for funding
503 Valentina Erastova and the Royal Society for funding H. Chris Greenwell. The work could not
504 have been completed without the use of Durham University's high-performance computing
505 services.

BIBLIOGRAPHY

- Aqvist, J. (1990). Ion-water interaction potentials derived from free energy perturbation simulations. *The Journal of Physical Chemistry*, **94**, 8021-8024.
- Barducci, A., Bussi, B. and Parrinello M. (2008). Well-Tempered Metadynamics: A Smoothly Converging and Tunable Free energy Method. *Physical Review Letters*, **100**, 020603.
- Benson, L.V. (1982). A tabulation and evaluation of ion exchange data on smectites. *Environmental Geology*, **4**, 23-29.
- Berendsen, H.J.C, Grigera, J.R. and Straatsma, T.P. (1987). The missing term in effective pair potentials. *The Journal of Physical Chemistry*, **91**, 6269–6271.
- Bergaya, F., Theng, B. and Lagaly, G. (2006). *Handbook of Clay Science (Vol. 1)*. Elsevier Science.
- Boek, E.S., Coveney, P.V. and Skipper, N.T. (1995). Monte Carlo Molecular Modeling Studies of Hydrated Li-, Na-, and K-Smectites: Understanding the Role of Potassium as a Clay Swelling Inhibitor. *The Journal of the American Chemical Society*, **117**, 12608–12617.
- Boek, E.S. and Sprik, M. (2003). Ab initio molecular dynamics study of the hydration of a sodium smectite clay. *The Journal of Physical Chemistry B*, **107**, 3251-3256.
- Bonomi, M., Branduardi, D., Bussi, G., Camilloni, C., Provasi, D., Raiteri, P., Donadio, D., Marinelli, F., Pietrucci, F., Broglia, R.A. and Parrinello, M. (2009). PLUMED: A portable plugin for free energy calculations with molecular dynamics. *Computer Physics Communications*, **180**, 1961-1972.
- Bowers, G.M., Bish, D.L. and Kirkpatrick, R.J. (2008). H₂O and cation structure and dynamics in expandable clays: 2H and 39K NMR investigations of hectorite. *The Journal of Physical Chemistry C*, **112**, 6430-6438.

- 529 Bourg I.C. and Sposito G. (2011). *Ion exchange phenomena; Handbook of Soil Science,*
530 *Properties and Processes (2nd Ed.).* CRC Press, Boca Raton.
- 531 Brown, D.R. and Kevan, L. (1988). Aqueous coordination and location of exchangeable copper
532 (2+) cations in montmorillonite clay studied by electron spin resonance and electron spin
533 echo modulation. *Journal of the American Chemical Society*, **110**, 2743-2748.
- 534 Chang, F.R.C., Skipper, N.T. and Sposito, G. (1995). Computer simulation of interlayer
535 molecular structure in sodium montmorillonite hydrates. *Langmuir*, **11**, 2734-2741.
- 536 Chen, C.C. and Hayes, K.F. (1999). X-ray absorption spectroscopy investigation of aqueous Co
537 (II) and Sr (II) sorption at clay–water interfaces. *Geochimica et Cosmochimica Acta*, **63**,
538 3205-3215.
- 539 Coveney, P.V. and Wan, S. (2016). On the calculation of equilibrium thermodynamic properties
540 from molecular dynamics. *Physical Chemistry Chemical Physics*, **DOI:**
541 10.1039/C6CP02349E.
- 542 Cygan, R.T., Liang, J.J. and Kalinichev, A.G. (2004). Molecular Models of Hydroxide,
543 Oxyhydroxide, and Clay Phases and the Development of a General Force Field. *The*
544 *Journal of Physical Chemistry B*, **108**, 1255-1266.
- 545 Downs, R.T. and Hall-Wallace, M. (2003). The American Mineralogist crystal structure database.
546 *American Mineralogist*, **88**, 247-250.
- 547 Eisenman, G. (1962). Cation selective glass electrodes and their mode of operation. *Biophysical*
548 *Journal*, **2**, 259-323.
- 549 Gast, R.G. (1972). Alkali metal cation exchange on Chambers montmorillonite. *Soil Science*
550 *Society of America Journal*, **36**, 14-19.

- 551 Gast, R.G. (1969). Standard free energies of exchange for alkali metal cations on Wyoming
552 bentonite. *Soil Science Society of America Journal*, **33**, 37-41.
- 553 Greathouse, J.A., Refson, K. and Sposito, G. (2000). Molecular dynamics simulation of water
554 mobility in magnesium-smectite hydrates. *Journal of the American Chemical Society*,
555 **122**, 11459-11464.
- 556 Greathouse, J.A., Hart, D.B., Bowers, G.M., Kirkpatrick, R.J. and Cygan, R.T. (2015). Molecular
557 Simulation of Structure and Diffusion at Smectite–Water Interfaces: Using Expanded
558 Clay Interlayers as Model Nanopores. *The Journal of Physical Chemistry C*, **119**, 17126–
559 17136.
- 560 Greenwell, H.C., Jones, W., Coveney, P.V. and Stackhouse, S. (2006). On the application of
561 computer simulation techniques to anionic and cationic clays: A materials chemistry
562 perspective. *Journal of Materials Chemistry* , **16**, 708-723.
- 563 Hanshaw, B.B. (1964). Cation-exchange constants for clays from electrochemical measurements.
564 *12th Annual Meeting of the Clay Minerals Society*.
- 565 Heinz, H., Lin, T.-J., Mishra, R.K. and Emami, F.S. (2013). Thermodynamically Consistent
566 Force Fields for the Assembly of Inorganic, Organic, and Biological Nanostructures: The
567 INTERFACE Force Field. *Langmuir*, **29**, 1754-1765.
- 568 Hunter, J.D. (2007). Matplotlib: A 2D graphics environment. *Computing in Science and*
569 *Engineering*, **9**, 90-95.
- 570 Koneshan, S., Lynden-Bell, R.M. and Rasaiah, J.C. (1998). Friction Coefficients of Ions in
571 Aqueous Solution at 25 °C. *The Journal of the American Chemical Society*, **120**, 12041-
572 12050.

- 573 Marry, V. and Turq, P. (2003). Microscopic simulations of interlayer structure and dynamics in
574 bihydrated heteroionic montmorillonites. *The Journal of Physical Chemistry B*, **107**,
575 1832-1839.
- 576 Marry, V., Dubois, E., Malikova, N., Breu, J. and Haussler, W. (2013). Anisotropy of water
577 dynamics in clays: insights from molecular simulations for experimental QENS analysis.
578 *The Journal of Physical Chemistry C*, **117**, 15106-15115
- 579 Michaud-Agrawal, N., Denning, E.J., Woolf, T.B. and Beckstein, O. (2011). MDAanalysis: a
580 toolkit for the analysis of molecular dynamics simulations. *Journal of Computational*
581 *Chemistry*, **32**, 2319-2327.
- 582 Nakano, M., Kawamura, K. and Ichikawa, Y. (2003). Local structural information of Cs in
583 smectite hydrates by means of an EXAFS study and molecular dynamics simulations.
584 *Applied Clay Science*, **23**, 15-23.
- 585 Ngouana W., B.F. and Kalinichev, A.G. (2014). Structural Arrangements of Isomorphic
586 Substitutions in Smectites: Molecular Simulation of the Swelling Properties, Interlayer
587 Structure, and Dynamics of Hydrated Cs–Montmorillonite Revisited with New Clay
588 Models. *The Journal of Physical Chemistry C*, **118**, 12758-12773.
- 589 Papelis, C. and Hayes, K.F. (1996). Distinguishing between interlayer and external sorption sites
590 of clay minerals using X-ray absorption spectroscopy. *Colloids and Surfaces A:*
591 *Physicochemical and Engineering Aspects*, **107**, 89-96.
- 592 Park, S.H. and Sposito, G. (2002). Structure of water adsorbed on a mica surface. *Physical*
593 *Review Letters*, **89**, 085501.
- 594 Pronk, S., Páll, S., Schulz, R., Larsson, P., Bjelkmar, P., Apostolov, R., Shirts, M.R., Smith, J.C.,
595 Kasson, P.M., van der Spoel, D. and Hess, B. (2013). GROMACS 4.5: a high-throughput

- 596 and highly parallel open source molecular simulation toolkit. *Bioinformatics*, **29**, 845-
597 854.
- 598 Rotenberg, B., Marry, V., Malikova, N. and Turq, P. (2010). Molecular simulation of aqueous
599 solutions at clay surfaces. *Journal of Physics: Condensed Matter*, **22**, 284114.
- 600 Rotenberg, B., Marry, V., Vuilleumier, R., Malikova, N., Simon, C. and Turq, P. (2007). Water
601 and ions in clays: Unraveling the interlayer/micropore exchange using molecular
602 dynamics. *Geochimica et Cosmochimica Acta*, **71**, 5089-5101.
- 603 Rotenberg, B., Morel, J.-P., Marry, V., Turq, P. and Morel-Desrosiers, N. (2009). On the driving
604 force of cation exchange in clays: Insights from combined microcalorimetry experiments
605 and molecular simulation. *Geochimica et Cosmochimica Acta*, **73**, 4034-4044.
- 606 Strawn, D.G. and Sparks, D.L. (1999). The use of XAFS to distinguish between inner-and outer-
607 sphere lead adsorption complexes on montmorillonite. *Journal of Colloid and Interface
608 Science*, **216**, 257-269.
- 609 Shroll, R.M. and Smith, D.E. (1999). Molecular dynamics simulations in the grand canonical
610 ensemble: Application to clay mineral swelling. *The Journal of Chemical Physics*, **111**,
611 9025-9033.
- 612 Smith, D.E. and Dang, L.X. (1994). Computer simulations of cesium–water clusters: Do ion–
613 water clusters form gas-phase clathrates? *The Journal of Chemical Physics*, **101**, 7873.
- 614 Smith, D.E. and Dang, L.X. (1994). Computer simulations of NaCl association in polarizable
615 water. *The Journal of Chemical Physics*, **100**, 3757.
- 616 Suter, J.L., Anderson, R.L., Greenwell, H.C. and Coveney, P.V. (2009). Recent advances in large-
617 scale atomistic and coarse-grained molecular dynamics simulation of clay minerals.
618 *Journal of Materials Chemistry*, **19**, 2482-2493.

- 619 Swenson, J., Bergman, R. and Howells, W.S. (2000). Quasielastic neutron scattering of two-
620 dimensional water in a vermiculite clay. *The Journal of Chemical Physics*, **113**, 2873-
621 2879
- 622 Teppen, B.J. and Miller, D.M. (2006). Hydration Energy Determines Isovalent Cation Exchange
623 Selectivity by Clay Minerals. *Soil Science Society of America Journal*, **70**, 31-40.
- 624 Tesson, S., Salanne, M., Rotenberg, B., Tazi, S. and Marry, V. (2016). Classical Polarizable Force
625 Field for Clays: Pyrophyllite and Talc. *The Journal of Physical Chemistry C*, **120**, 3749-
626 3758.
- 627 Tribello, G.A., Bonomi, M., Branduardi, D., Camilloni, C. and Bussi, G. (2014). PLUMED 2:
628 New feathers for an old bird. *Computer Physics Communications*, **185**, 604-613.
- 629 Underwood, T., Erastova, V., Cubillas, P. and Greenwell, H.C. (2015). Molecular Dynamic
630 Simulations of Montmorillonite–Organic Interactions under Varying Salinity: An Insight
631 into Enhanced Oil Recovery. *The Journal of Physical Chemistry C*, **119**, 7282–7294.
- 632 Viani, A., Gualtieri, A.F. and Artioli, G. (2002). The nature of disorder in montmorillonite by
633 simulation of X-ray powder patterns. *American Mineralogist*, **87**, 966-975.
- 634 William Humphrey, A.D. (1996). VMD: visual molecular dynamics. *Journal of Molecular*
635 *Graphics*, **14**, 33-38.
- 636 Zhang, P.C., Brady, P.V., Arthur, S.E., Zhou, W.Q., Sawyer, D. and Hesterberg, D.A. (2001).
637 Adsorption of barium (II) on montmorillonite: an EXAFS study. *Colloids and Surfaces A:*
638 *Physicochemical and Engineering Aspects*, **190**, 239-249.
- 639 Zhang, Y. and Cremer, P.S. (2006). Interactions between macromolecules and ions: the
640 Hofmeister series. *Current Opinion in Chemical Biology*, **10**, 658-663.
- 641

Table 1

Binding energies and stable clay-ion separations of cations to montmorillonite basal surfaces. The global energy minimum for each ion is bolded. Clay-ion separation values are given in Angstrom and Binding Energies are in kJ/mol. The Primary ISSC is defined as the inner-sphere complex located above the hexagonal siloxane cavity of the clay, whilst the secondary ISSC is the complex above a basal surface oxygen.

Ion	VdW Radii	Primary ISSC		Secondary ISSC		OSSC		SHSSC	
		Separation	Energy	Separation	Energy	Separation	Energy	Separation	Energy
Na ⁺	2.35	-		2.3	-2.76 (0.43)	3.8	-9.00 (0.35)	6.0	-3.68 (0.37)
K ⁺	3.33	1.3	-10.56 (1.29)	2.6	-2.46 (0.70)	4.7	-3.83 (0.37)	-	
Cs ⁺	3.83	2.0	-8.34 (0.40)	2.7	-7.51 (0.38)	4.6	-4.64 (0.26)	-	
Ca ²⁺	2.87	-		-		3.8	-16.76 (0.41)	-	
Ba ²⁺	3.81	1.9	+18.26 (3.55)	2.6	-0.54 (1.82)	4.2	-16.66 (1.46)	5.8	-8.38 (1.25)

Table 2

The atomic radii and therefore charge to size ratio for each ion. The hydrated radii are calculated as the first minima in the RDF of each respective ion. The stable surface complex of each ion is linked to the size of the ion's hydration radii and thus charge to size ratio.

Ion	Atomic Radii	Charge/Size ratio	Hydrated Radii	Stable Complex
Na ⁺	1.90	0.53	3.23	OSSC
K ⁺	2.43	0.41	3.83	ISSC
Cs ⁺	2.98	0.34	3.87	ISSC
Ca ²⁺	1.94	1.03	3.13	OSSC
Ba ²⁺	2.53	0.79	3.49	OSSC

Table 3

The coordination number of each ion in each surface complexation state. Expected coordination numbers are taken from (Varma, 2006).

Species	Expected CN	Observed CN	Clay CN	Water CN	Percentage Clay	Percentage Water
<i>Primary ISSC</i>						
Na ⁺	5	-	-	-	-	-
K ⁺	6	9.3	5.9	3.4	64%	36%
Cs ⁺	7	11.8	5.9	5.9	50%	50%
Ca ²⁺	5-7	-	-	-	-	-
Ba ²⁺	5-7	8.5	1.1	7.4	13%	87%
<i>Secondary ISSC</i>						
Na ⁺	5	5.9	1.1	4.8	19%	81%
K ⁺	6	7.6	1.9	5.7	25%	75%
Cs ⁺	7	9.4	2.7	6.7	29%	71%
Ca ²⁺	5-7	-	-	-	-	-
Ba ²⁺	5-7	8.5	1.1	7.4	13%	87%
<i>OSSC</i>						
Na ⁺	5	5.9	0	5.9	0%	100%
K ⁺	6	7.6	0	7.6	0%	100%
Cs ⁺	7	9.3	0	9.3	0%	100%
Ca ²⁺	5-7	8	0	8	0%	100%
Ba ²⁺	5-7	9	0	9	0%	100%
<i>SHSSC</i>						
Na ⁺	5	5.8	0	5.8	0%	100%
K ⁺	6	-	-	-	-	-
Cs ⁺	7	-	-	-	-	-
Ca ²⁺	5-7	8	0	8	0%	100%
Ba ²⁺	5-7	9	0	9	0%	100%
<i>Bulk</i>						
Na ⁺	5	5.9	0	5.9	0%	100%
K ⁺	6	7.8	0	7.8	0%	100%
Cs ⁺	7	8.2	0	8.2	0%	100%
Ca ²⁺	5-7	8	0	8	0%	100%
Ba ²⁺	5-7	9	0	9	0%	100%

Table 4

The binding energy difference ($\Delta\Delta G_A^B$) between ion species.

$\Delta\Delta G_A^B$	Na ⁺	K ⁺	Cs ⁺	Ca ²⁺	Ba ²⁺
Na ⁺	0.00	-1.56	0.66	0.62	0.67
K ⁺	1.56	0.00	2.22	2.18	2.23
Cs ⁺	-0.66	-2.22	0.00	-0.04	0.01
Ca ²⁺	-0.62	-2.18	0.04	0.00	0.05
Ba ²⁺	-0.67	-2.23	-0.01	-0.05	0.00

Table 5

The exchange equilibrium constants ($^{\text{ex}}K_A^B$) for each ion exchange reaction. Literature values are presented in bold italics (Bourg and Sposito, 2011) (Benson, 1982).

$^{\text{ex}}K_A^B$	Na ⁺	K ⁺	Cs ⁺	Ca ²⁺	Ba ²⁺
Na ⁺	-	1.87	0.77	0.78	0.76
K ⁺	0.54 0.58	-	0.41	0.42	0.41
Cs ⁺	1.30 1.23	2.44	-	1.02	1.00
Ca ²⁺	1.28 1.21	2.40 1.04	0.98 0.26	-	0.98
Ba ²⁺	1.31 1.44	2.45	1.00	1.02	-

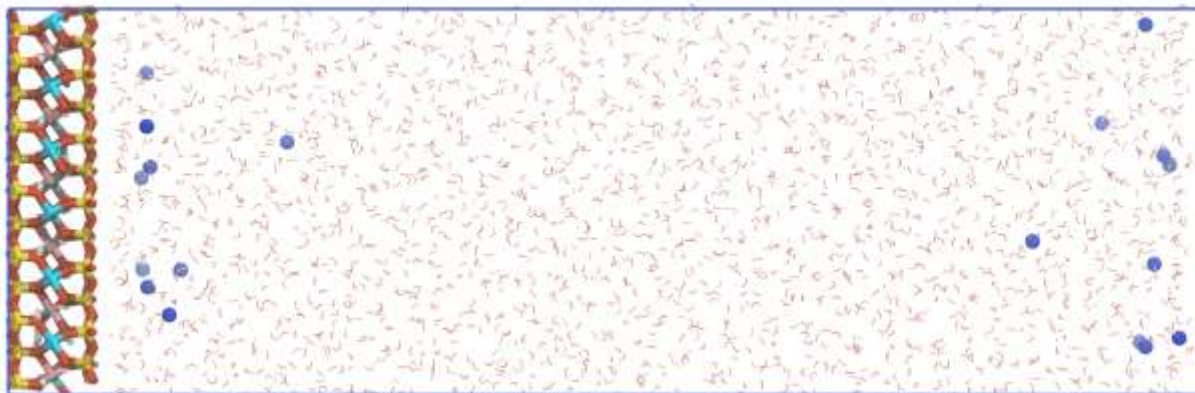


Figure 1: An example supercell used in the simulations. This example is of sodium cations (dark blue) interacting with montmorillonite. The color scheme of the clay is as follows: Silicons are yellow; oxygens are red; aluminums are blue; magnesiums are pink and hydrogens are white. Also presented in stick form are the water molecules within the nano-pore spacing. Periodic boundaries are used in all directions, and the simulation supercell has dimensions approximately $4 \times 4 \times 10$ nm (note that the figure is flipped here, such that the z -direction is across the page, from left to right).

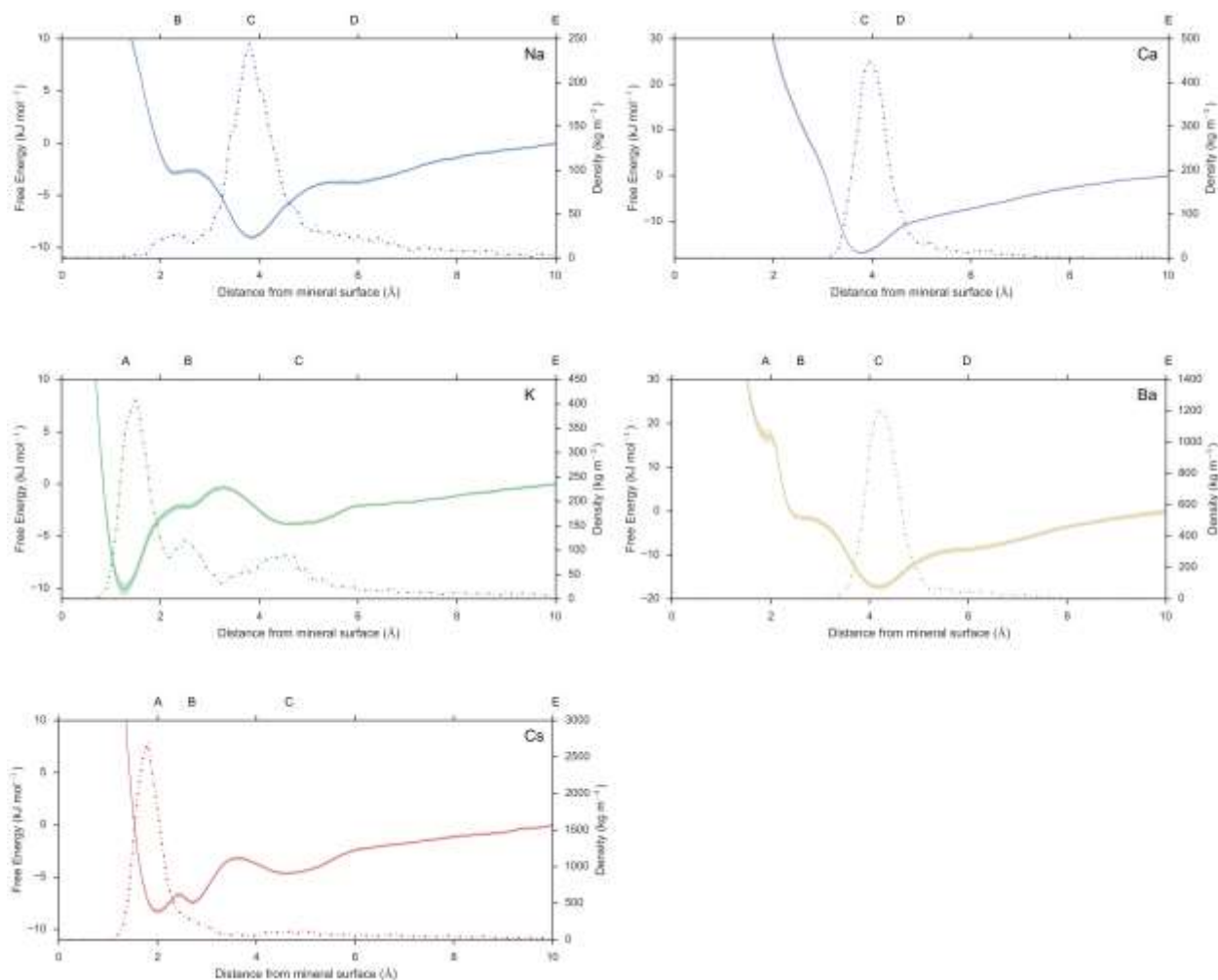


Figure 2: The free energy profile of all cations as a function of clay-ion separation. Note that the shaded region indicates the standard error in the metadynamic calculation at each point along the free-energy diagram. Also presented is the ion density as a function of distance from clay basal surface (dotted line). The points (A), (B), (C) and (D) are noted as interesting features within the free-energy diagram and are shown at the top of the figure.

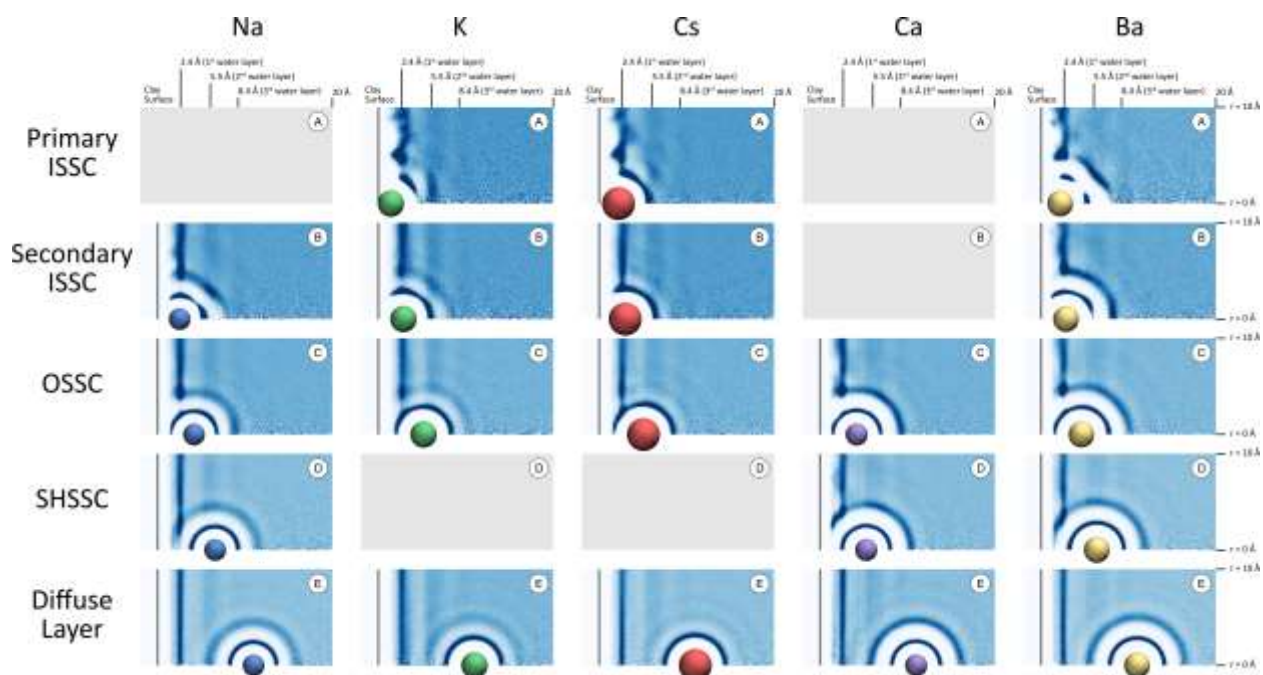


Figure 3: The water oxygen density surrounding the clay and ion at point of interest along the free-energy curve.

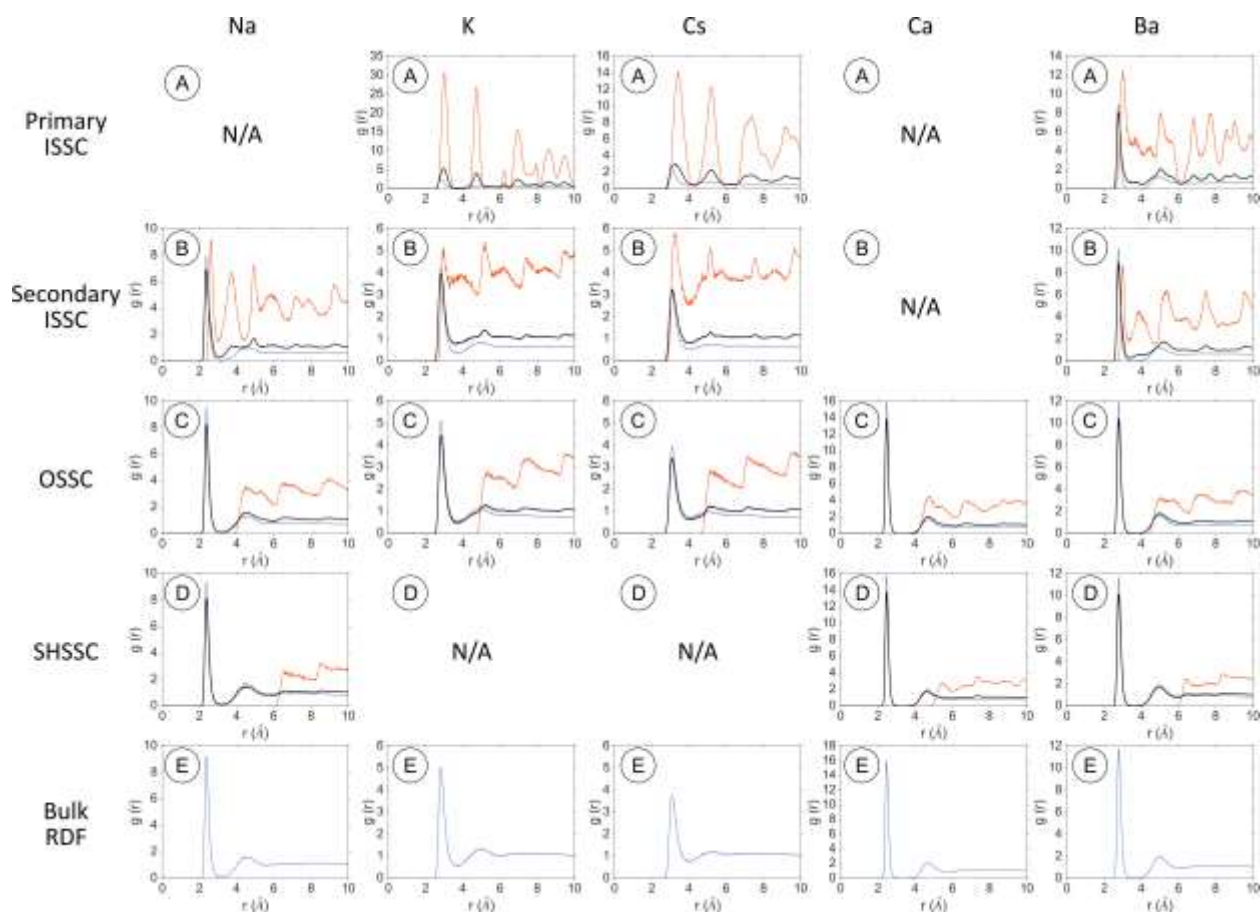


Figure 4: The RDF's between each cation and oxygen atoms at each point of interest along the free-energy diagram. Blue is the RDF between cation and water oxygen, orange is between cation and clay oxygen, and black is the RDF between cation and all oxygen atoms.

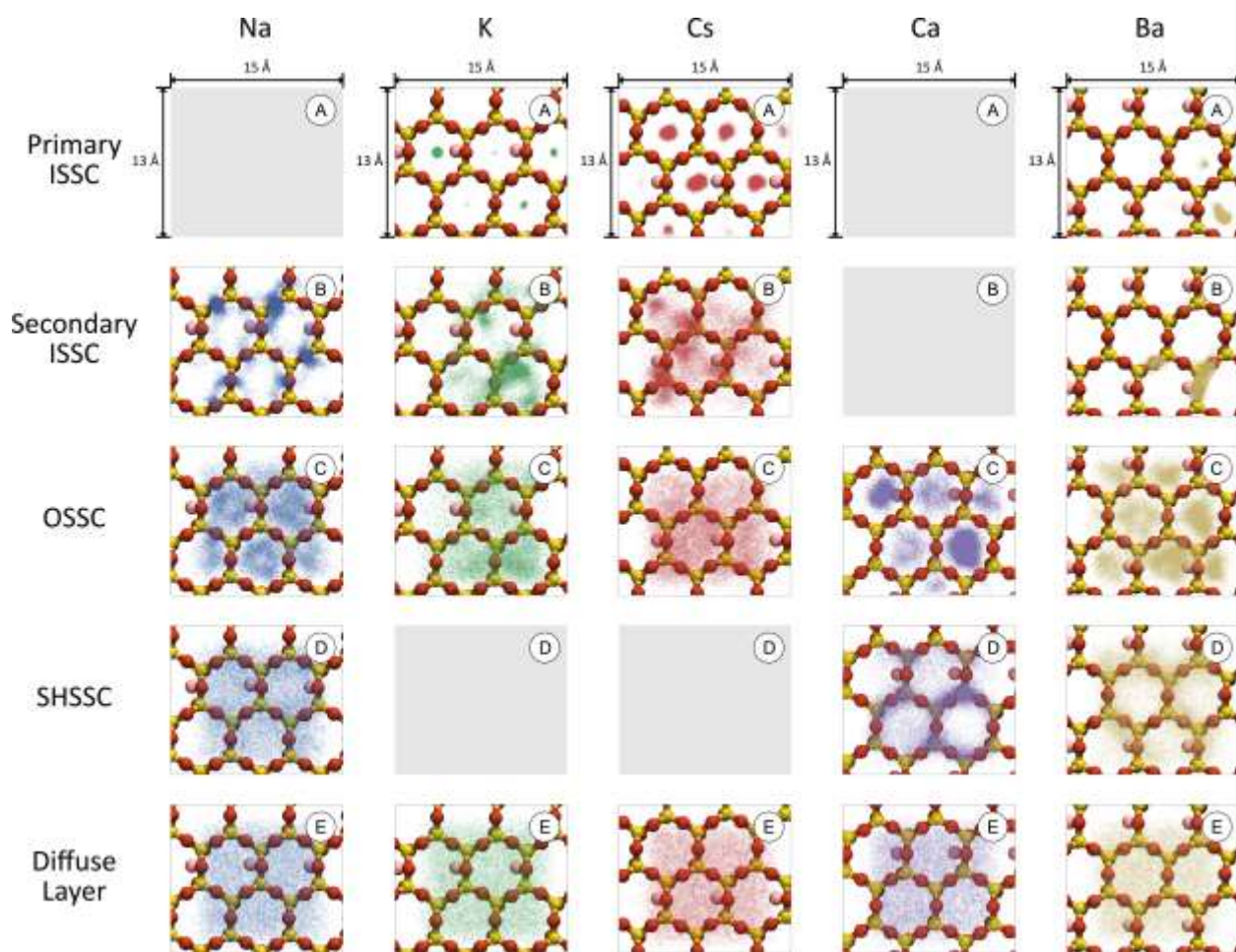


Figure 5: The xy-planar density of the examined cations at each point of interest along the free energy curve.

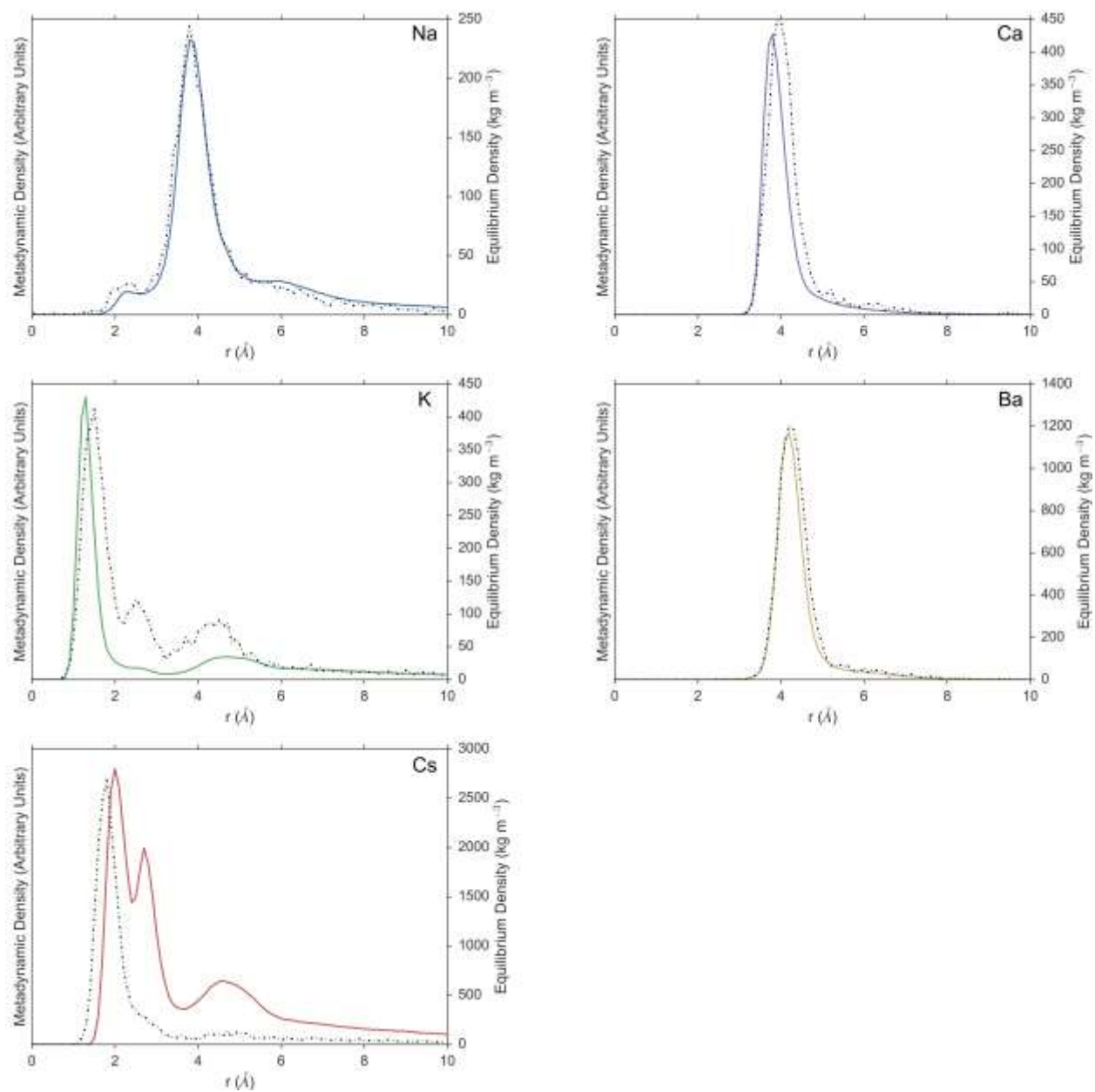


Figure 6: A comparison of ionic densities surrounding the clay surface. Bold colored line is the density calculated from the free energy profile, and the dotted line is the density calculated from an unbiased simulation.